Use of spatiotemporal couplings and an axiparabola to control the velocity of peak intensity

Aaron Liberman, Ronan Lahaye, Slava Smartsev, Sheroy Tata, Salome Benracassa, Anton Golovanov, Eitan Levine, Cedric Thaury, Victor Malka

Optics Letters

Use of spatiotemporal couplings and an axiparabola to control the velocity of peak intensity

Aaron Liberman,[1,*] Ronan Lahaye,[2] Slava Smartsev,[1,2] Sheroy Tata,[1] Salome Benracassa,[1] Anton Golovanov,[1] Eitan Levine,[1] Cedric Thaury,[2] and Victor Malka[1]

[1]Department of Physics of Complex Systems, Weizmann Institute of Science, Rehovot 7610001, Israel
[2]LOA, CNRS, Ecole Polytechnique, ENSTA Paris, Institut Polytechnique de Paris, Palaiseau, France
*aaronrafael.liberman@weizmann.ac.il

Received 9 October 2023; revised 22 December 2023; accepted 24 December 2023; posted 2 January 2024; published 5 February 2024

This paper presents the first experimental realization of a scheme that allows for the tuning of the velocity of peak intensity of a focal spot with relativistic intensity. By combining a tunable pulse-front curvature with the axial intensity deposition characteristics of an axiparabola, an aspheric optical element, this system provides control over the dynamics of laser-wakefield accelerators. We demonstrate the ability to modify the velocity of peak intensity of ultrashort laser pulses to be superluminal or subluminal. The experimental results are supported by theoretical calculations and simulations, strengthening the case for the axiparabola as a pertinent strategy to achieve more efficient acceleration.

https://doi.org/10.1364/OL.507713

With the proliferation of femtosecond, multi-terawatt pulses, high-power laser systems have become an essential tool in scientific research. In particular, such laser systems, when coupled to plasma, can produce a compact particle accelerator, capable of generating high-quality proton, electron, and x ray beams [1–4]. One such accelerator type, laser-wakefield accelerators (LWFAs) [5] – high gradient accelerators in which electrons are trapped and accelerated in laser-generated plasma wakes – can produce GeV energy-scale electrons in centimeter-sized acceleration lengths [6]. LWFAs promise to contribute to many applications, including cancer treatments [7] and next-generation light sources [8]. There remain, however, a number of limitations that prevent the achievement of ever higher energies [9]. These include the tendency of the laser to diffract [9] – requiring guiding mechanisms to remain in focus [10] – and the dephasing of the electrons from the wakefield [9], potentially ending the acceleration before the laser is depleted [11].

The axiparabola, a long-focal-depth reflective optical element that produces a quasi-Bessel beam [12], has generated interest for its potential to overcome both beam diffraction and electron dephasing [13,14]. Beam diffraction can be overcome by the diffraction mitigating propagation properties of the Bessel beam, which have been used to generate a high-quality waveguide for LWFA [15]. The axiparabola tackles the dephasing issue through a combination of the peak intensity propagation dynamics imposed by the axiparabola itself and a manipulation of the pulse-front curvature (PFC) of the incoming beam [13,14]. Through this combination, the velocity of peak intensity can be tuned from subluminal (v<c) to superluminal (v>c), allowing the wakefield to be phase-locked to the electron beam. This paper presents the first experimental realization of a system that promises to utilize the properties of the axiparabola in order to achieve dephasingless acceleration. The manipulation of the energy deposition velocity is achieved by combining an axiparabola and a refractive doublet that modifies the PFC of the beam. The experiment was performed with the HIGGINS 100 TW laser system at the Weizmann Institute of Science, which produces nearly top-hat, 30 fs, 50 mm diameter pulses [16].

While superluminal energy deposition has been previously demonstrated [17–19], this is the first experiment, to our knowledge, that shows its feasibility using the axiparabola and, thus, presents a road map for further optimization toward the eventual goal of dephasingless laser-wakefield acceleration. The axiparabola-based approach, unlike the chromatic flying focus [19,20], yields an ultrashort pulse duration since it does not add chirp to the pulse. The axiparabola-based method is a promising, experimentally simpler way to achieve dephasingless acceleration.

The axiparabola has a radially dependent focal length, $f(r)$, with different annular segments focusing at different points on the focal line over a segment known as the focal depth. A detailed description of the axiparabola can be found in [12,21]. By causing light at different radial distances to have different path lengths to the optical axis, the axiparabola introduces a radially dependent focusing time, $t(r)$, and thus modifies the velocity of the on-axis intensity propagation, $v_z = df/dt$ [13,14]. Here, $z = f - f_0$, where f_0 is the nominal focal length of the axiparabola. Using ray optics and paraxial approximations, the velocity is $v_z/c = 1 + r^2/2f^2$ [14]. If the pulse incident on the axiparabola has a radial delay $\tau(r)$, the velocity is modified [21]:

$$\frac{v_z'}{c} = \frac{v_z}{c}\left(1 - \frac{v_z}{c} c \frac{d\tau}{dr}\frac{dr}{dz}\right). \tag{1}$$

This experiment used an axiparabola with the focal line distribution: $f(r) = f_0 + \delta(r/R)^2$, where $\delta>0$ is the focal depth and R is the total radius of the pulse. For such an axiparabola, and with a radial delay caused by the pulse-front curvature of $\tau(r) = \alpha r^2$, the modified velocity, up to second-order terms becomes

$$\frac{v_z'}{c} = 1 - \frac{c\alpha R^2}{\delta} + \left(\frac{R^2}{2\delta f_0^2} - \frac{c\alpha R^4}{\delta^2 f_0^2}\right)z - \left(\left[\frac{R^2}{2\delta f_0^2} - \frac{c\alpha R^4}{\delta^2 f_0^2}\right]\frac{2}{f_0} - \frac{c\alpha R^6}{2\delta^3 f_0^4}\right)z^2. \quad (2)$$

A more complete derivation may be found in Supplement 1.

The pulse-front curvature of the HIGGINS laser was measured using far-field beamlet cross-correlation (FFBCC) [22], a self-referenced technique that utilizes far-field interferometry and inverse Fourier transform spectroscopy. The method works by scanning the delay between two beamlets and using the interference obtained by focusing them with a parabola to extract the relative pulse delay. In the case of this PFC measurement, a 2 m off-axis parabola was used. Repeating this for different sections of the beam maps the pulse-front delay [22].

The PFC control doublet, a lens designed to cancel out the PFC which is introduced in the laser system due to the refractive telescopes used to expand the beam [23], was placed inside of the final telescope expansion stage of the laser. Details of the doublet are provided in [22]. The doublet's effect scales with the size of the beam impinging on the doublet [24]. Thus, by changing the doublet's position inside the telescope, the PFC of the beam can be controlled in amplitude and direction without changing the focal plane and with minimal added aberrations. The PFC of the laser chain was simulated using the Zemax OpticStudio ray-tracing software. Two custom macros were used, one to calculate the pulse-front delay and the other to simulate the intensity over the focal depth. Details can be found in [25].

All experimental data was taken with the HIGGINS 100 TW laser system. The laser was fully amplified and then attenuated from 3 J to 8 μJ, so as not to damage the objective and CCD. Apart from the focal spot diagnostics needed for FFBCC, which are not necessary for an electron acceleration experiment, the setup can be used with the full power beam. With no attenuation, the B-integral through the doublet is orders of magnitude below that which would result in significant nonlinear effects.

In the PFC measurement, three doublet positions inside of the beam expansion telescope were used: 0 mm (directly after the first lens), 65 mm, and 130 mm (middle point between lenses). The modification of the PFC by the doublet increases with larger values of the position inside the telescope as the beam's size grows. Data without the doublet was also taken. Figure 1 shows the Zemax simulated PFC coefficient α (orange) as well as the experimentally obtained values for the 0 mm (blue), 65 mm (red), and 130 mm (cyan) doublet positions and the no doublet case (green). These values correspond to the α of Eq. (2). The insets show the measured pulse-front delays. The dots are the measured values for the pulse-front delay at that spatial point, with the width of the dot showing the experimental error bar. The colored surface shows the PFC fit of the radial delay. As shown in the figure, the range of PFC allowed by moving the doublet in the telescope gives the ability to partially and fully suppress, and even invert, the PFC inherent in the refractive beam expansion. Full suppression of the PFC takes place at a doublet position around 75 mm. The simulations for the doublet-in cases agree with the experimentally obtained values, while the no-doublet case deviates slightly, likely due to experimental errors such as mask misalignment.

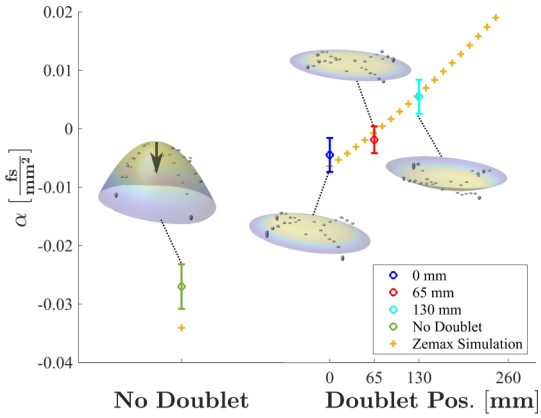

Fig. 1. Zemax simulated (orange) and measured PFC coefficient α for 0 mm (blue), 65 mm (red), and 130 mm (cyan) doublet positions and the no doublet case (green). The insets show the measured pulse-front delays. The dots are the measured values for the pulse-front delay at that spatial point, with the width of the dot showing the experimental error bar. The colored surface shows the PFC fit of the radial delay. Black arrow shows the propagation direction of the pulse.

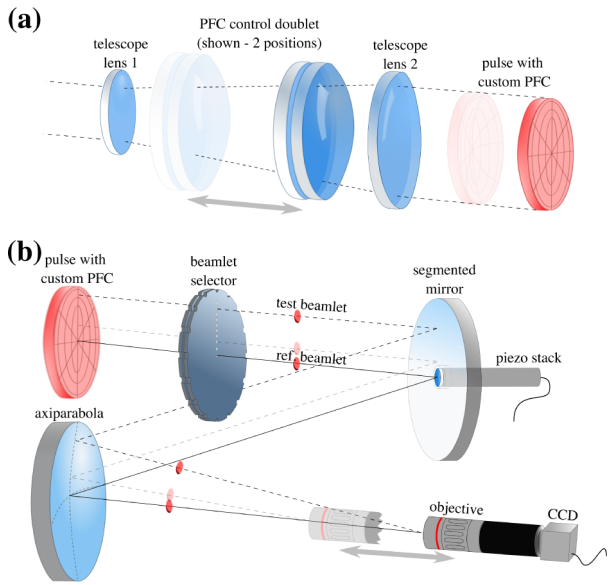

Fig. 2. (a) Setup of the PFC control doublet inside the final beam expansion stage for two positions and with two resultant PFC values for the beam. (b) Group velocity measurement setup in which the beam impinges on the selector and the reference and test beamlets pass through. The segmented mirror imparts a tunable delay to the reference beamlet. Both beamlets are focused on the axiparabola, and the interference is imaged onto a CCD through an objective. Two radial offsets of the test beamlet are shown.

The axiparabola group velocity measurement, an overview of which is shown in Fig. 2, was performed in air and was based on a modified version of FFBCC. The measurement of the energy deposition velocity utilized a specially designed beamlet selector mask that selects a test beamlet from a radially and angularly tunable section of the beam and selects the central reference beamlet. A variable delay is added to the reference beamlet by impinging the beamlets onto a segmented mirror whose central

section is attached to a piezo actuator. The beamlets were then focused by the axiparabola, and the resultant interference was imaged using an objective and CCD. The imaging system was moved to coincide with the focus of the test and reference beamlets, and a delay scan was performed for four radial offset values. The resulting value for the delay difference for each radial slice was extracted by finding the relative delay needed to achieve maximum contrast of the interference of the two beamlets. Since the reference beamlet at $r = 0$ corresponds to the place where the average of the $\vec{k}$'s for all other points is 0, the relative delay of the test beamlet is taken as deviation from a luminal arrival time. The data for the different test beamlet values was fitted, and the derivative of this fit function yields the difference between the velocity of peak intensity and the speed of light. For more details on this analysis, see Supplement 1. Simulations were also done to verify that the objective introduced negligible chromatic dispersion and thus did not introduce radial delay.

The axiparabola had a nominal focal length of 480 mm, a focal depth of 5 mm, and an off-axis angle of 10°. It was designed to have a quasi-constant intensity over the focal depth. Due to the relatively short focal depth chosen for these proof-of-concept experiments, interference effects led to an intensity profile with two peaks along the focal depth. As shown in an earlier work [21] and in a recent article [26], these modulations come from diffraction of the spherically aberrated phase fronts, an effect which goes beyond the geometric optics approximation. For future acceleration experiments, an axiparabola with a higher ratio of focal depth to Rayleigh range will be used, helping mitigate these effects [26]. Figure 3 shows both the Zemax OpticStudio simulation (red) and the experimentally obtained (blue) intensity of the axiparabola central spot over the focal depth. Insets show the measured focal spot at different z values, illustrating the development of the Bessel ring structures. The second peak of the intensity profile is experimentally reduced relative to the simulation due to spatial aberrations. These appear because the end of the focal depth is generated by large aperture annuli and is thus more susceptible to aberrations [12]. For the fully amplified, non-attenuated beam, we could expect a peak intensity of the axiparabola focused beam of around $2.2 \times 10^{19}\mathrm{W/cm}^2$.

Experimental data was first taken without the PFC control doublet in the laser chain. The control doublet was then introduced. By manipulating the PFC of the beam incoming

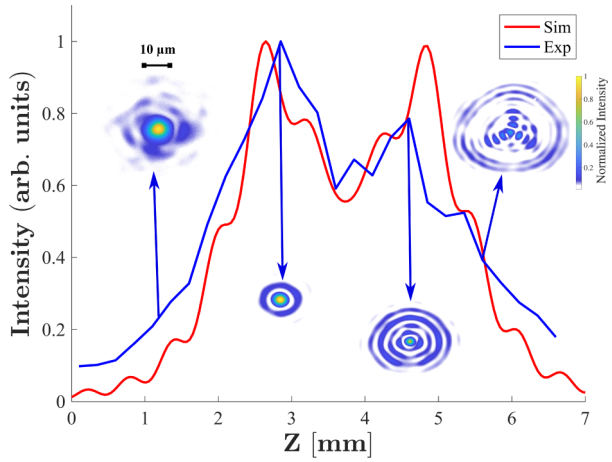

Fig. 3. Peak intensity over the focal depth, showing both Zemax simulated (red) and experimental data (blue). The insets show 2D focal spot images at specified points.

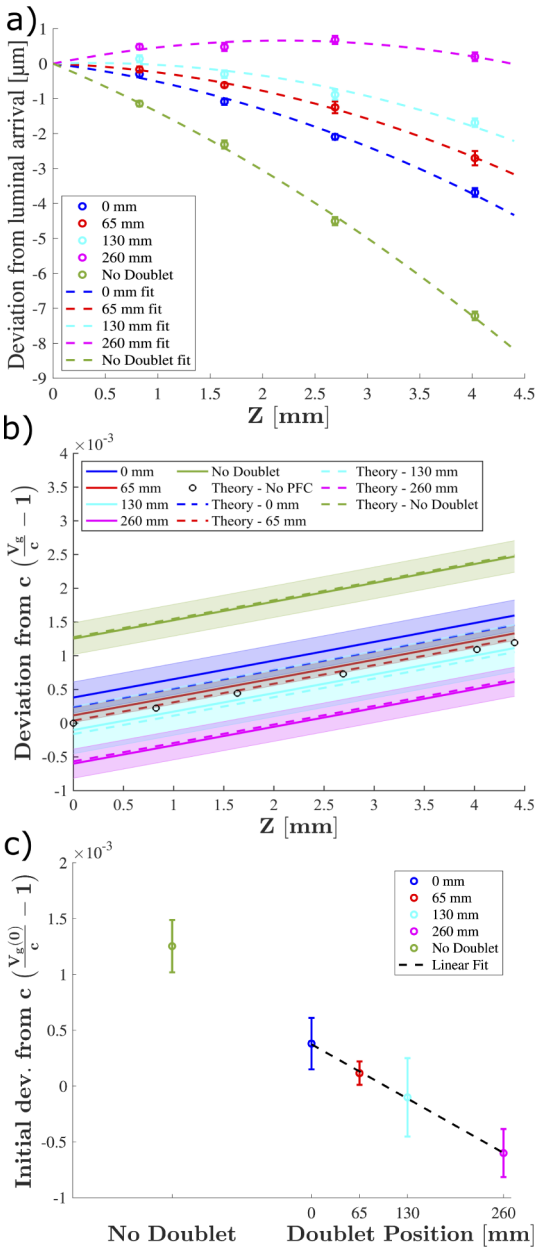

Fig. 4. (a) Deviation of the annular sections of the axiparabola from luminal propagation in the no doublet (green), 0 mm (blue), 65 mm (red), 130 mm (cyan), and 260 mm (magenta) cases. The dotted line shows the fit. (b) Negative derivative of the fit functions shown in part a, with the shaded sections showing the error bars, the dotted lines showing the theory fits, and the black circles showing the no-PFC theory. (c) Initial deviation from the 0 PFC velocity for different doublet positions, with the dotted line showing the linear fit.

on the axiparabola, the doublet changes the relative timing of arrival of different radial segments of the laser to the axiparabola and thus the timing of the peak intensity propagation.

The results of the scan of the relative delay between the luminal propagation and the arrival of the annular sections of the axiparabola are shown in Fig. 4(a). The results are shown for data taken at focal positions $z = 0.8, 1.6, 2.7, 4.0$ mm, which correspond to the focusing points of the axiparabola annular

sections at radial values $r = 10.3, 14.5, 18.6, 22.8$ mm, respectively. These are the radial values of the test beamlets selected by the beamlet selector mask. Data is shown for the case where no PFC control doublet is in the laser chain (green), as well as when the doublet is at the 0 mm (blue), 65 mm (red), 130 mm (cyan), and 260 mm (magenta) positions inside of the final beam expander.

The deviation data was fit using a third-order polynomial fit function:

$$\mathrm{d}(z) = p_1 z^3 + p_2 z^2 + p_3 z + p_4, \quad \textbf{(3)}$$

where d is the deviation, to match the integral of the velocity equation shown in Eq. (2). Since each experimental fit had few points and the expectation is that the dominant contribution to the velocity change will come from the $p_3 z$ term, the values of p_1 and p_2 were taken to be the theoretical values given by the Zemax simulated PFC shown in Fig. 1, and the fit was used to obtain the values of p_3 and p_4. The experimental error bars show the error from the poor spatial resolution of the FFBCC measurement.

From the derivative of the group velocity from c was obtained from the derivative of the fit function in Eq. (3). The results are shown in Fig. 4(b). As expected, for the no-PFC control doublet case (green), the PFC inherent in the refractive beam expansion causes the largest superluminal velocity. When the doublet is introduced at 0 mm (blue), the starting position of the velocity is reduced. As the doublet is moved forward in the telescope to 65 mm (red), 130 mm (cyan), and 260 mm (magenta), the starting value of the velocity is further reduced. As the PFC of the beam is flipped in direction, between the doublet 65 mm and 130 mm positions, the starting velocity switched from superluminal to subluminal, as is expected from Eq. (2). The shaded regions are the error bars for each measurement. The dotted line of each color represents the theoretical expectation of the velocity, obtained from Eq. (2), where the PFC values used are extracted from the Zemax simulations. The theory agrees quite well with the experimental data, falling well within the error boundaries. The figure also shows the theoretical value for no PFC (black circles), which, as expected, falls between the doublet 65 mm and 130 mm positions, where α changes sign.

Figure 4(c) shows the difference in the starting ($z = 0$) velocity of the different doublet positions from the velocity with no PFC. The left side shows the no doublet case (green), while the right shows a graph with the different doublet positions (same coloring as before). The black dotted line shows the linear fit of the experimentally measured data as a function of the doublet position. This figure highlights the dynamic range in velocity control afforded by the PFC manipulation.

This paper presents the first experimental realization of an axiparabola-based scheme for tuning the axial deposition velocity. The dynamic range shown in the velocity measurements allows for the easy transition between superluminal, luminal, and subluminal velocities. These results confirm that the axiparabola behaves as expected, both in focal spot intensity over the focal depth and in velocity. With the axiparabola characterized and the velocity manipulation demonstrated, this setup is now ready to facilitate the first high-power axiparabola-based attempts at dephasingless laser-wakefield acceleration.

Since these results were first presented, similar results have been obtained and published in a conference proceeding [27].

Funding. Schwartz/Reisman Center for Laser Physics; Benoziyo Endowment Fund for the Advancement of Science; Israel Science Foundation; Minerva Foundation; Wolfson Foundation; Schilling Foundation; R. Lapon; Dita and Yehuda Bronicki; Helmholtz Association.

Disclosures. The authors declare no conflicts of interest.

Data availability. Data available upon reasonable request to the authors.

Supplemental document. See Supplement 1 for supporting content.

REFERENCES

1. S. P. D. Mangles, C. D. Murphy, Z. Najmudin, *et al.*, Nature **431**, 535 (2004).
2. C. G. R. Geddes, C. Toth, J. van Tilborg, *et al.*, Nature **431**, 538 (2004).
3. J. Faure, Y. Glinec, A. Pukhov, *et al.*, Nature **431**, 541 (2004).
4. V. Malka, J. Faure, Y. A. Gauduel, *et al.*, Nat. Phys. **4**, 447 (2008).
5. T. Tajima and J. M. Dawson, PRL **43**, 1 (1979).
6. A. J. Gonsalves, K. Nakamura, J. Daniels, *et al.*, Phys. Rev. Lett. **122**, 084801 (2019).
7. Y. Glinec, J. Faure, V. Malka, *et al.*, Med. Phys. **33**, 155 (2006).
8. W. Wang, K. Feng, L. Ke, *et al.*, Nature **595**, 516 (2021).
9. E. Esarey, C. B. Schroeder, and W. P. Leemans, Rev. Mod. Phys. **81**, 1229 (2009).
10. W. P. Leemans, A. J. Gonsalves, H.-S. Mao, *et al.*, Phys. Rev. Lett. **113**, 245002 (2014).
11. B.-S. Xie, H.-C. Wu, H. Wang, *et al.*, Phys. Plasmas **14**, 1 (2007).
12. S. Smartsev, C. Caizergues, K. Oubrerie, *et al.*, Opt. Lett. **44**, 3414 (2019).
13. J. P. Palastro, J. L. Shaw, D. Ramsey, *et al.*, Phys. Rev. Lett. **124**, 134802 (2020).
14. C. Caizergues, S. Smartsev, V. Malka, *et al.*, Nat. Photonics **14**, 475 (2020).
15. K. Oubrerie, A. Leblanc, O. Kononenko, *et al.*, Light: Sci. Appl. **11**, 180 (2022).
16. E. Kroupp, S. Tata, Y. Wan, *et al.*, Matter Radiat. Extremes **7**, 1 (2022).
17. D. Mugnai, A. Ranfagni, and R. Ruggeri, Phys. Rev. Lett. **84**, 4830 (2000).
18. I. Alexeev, K. Y. Kim, and H. M. Milchberg, Phys. Rev. Lett. **88**, 073901 (2002).
19. D. H. Froula, D. Turnbull, A. S. Davies, *et al.*, Nat. Photonics **12**, 262 (2018).
20. A. Sainte-Marie, O. Gobert, and F. Quere, Optica **4**, 1298 (2017).
21. K. Oubrerie, I. A. Andriyash, R. Lahaye, *et al.*, J. Opt. **24**, 045503 (2022).
22. S. Smartsev, S. Tata, A. Liberman, *et al.*, J. Opt. **24**, 115503 (2022).
23. R. Netz and T. Feurer, Appl. Phys. B **70**, 813 (2000).
24. A. Kabacinski, K. Oubrerie, J.-P. Goddet, *et al.*, J. Opt. **23**, 06LT01 (2021).
25. S. Smartsev, "Boosting electron beam energy in laser-plasma accelerators with plasma channel guiding," Thesis (Weizmann Institute of Science, 2022).
26. M. V. Ambat, J. L. Shaw, J. J. Pigeon, *et al.*, Opt. Express **31**, 31354 (2023).
27. J. J. Pigeon, P. Franke, M. L. P. Chong, *et al.*, *CLEO 2023* (Optica Publishing Group, 2023), paper FW3M.1.